Vacancy-assisted phase separation with asymmetric atomic mobility: Coarsening rates, precipitate composition, and morphology

Jean-Marc Roussel and Pascal Bellon
Department of Materials Science and Engineering and Frederick Seitz Materials Research Laboratory, University of Illinois at Urbana-Champaign, Urbana, Illinois 61801

(Received 15 September 2000; revised manuscript received 19 December 2000; published 24 April 2001)

We have investigated the coarsening kinetics and the morphology of precipitates after quenching a dilute binary alloy into its miscibility gap. Three-dimensional kinetic Monte Carlo simulations with a vacancy-diffusion mechanism are performed. The atomic diffusion model accounts for the asymmetry of the two terminal phases with respect to the vacancy concentration and diffusivity. It is shown that, at a fixed low temperature of about $0.25T_c$, this asymmetry has a profound effect on the mechanism responsible for precipitate coarsening and on precipitate morphology. For positive asymmetry (i.e., when the vacancy is mostly diffusing inside the precipitates), precipitate diffusion and coagulation are favored. Nearly pure solute precipitates with atomically sharp interfaces are formed in a persistently supersaturated matrix. For negative asymmetry (i.e., when the vacancy is mostly diffusing in the matrix), the evaporation condensation of solute atoms becomes dominant even at early stages. The lack of interfacial mobility produces disordered, diffuse interfaces, which then result in highly supersaturated precipitates. These last results offer an explanation to recent atomic observations of the precipitate morphology in the Cu-Co system. A mean-field model is introduced to rationalize how the asymmetry parameter controls the distribution of vacancies in a two-phase alloy. This model predicts that cluster mobility increases when the asymmetry parameter is increased, resulting in an increase of the coagulation exponent in agreement with the simulations. Furthermore, this model offers a rationalization for persistent supersaturations of the matrix or the precipitates, and this provides some insight into the formation of diffuse interfaces.

DOI: 10.1103/PhysRevB.63.184114 PACS number(s): 64.75.+g, 81.30.Mh, 66.30.−h, 68.35.Fx

I. INTRODUCTION

When a dilute disordered alloy is quenched into a miscibility gap, precipitates form and grow in size. This apparently simple transformation has received considerable attention, both from an experimental and theoretical viewpoint.[1,2] Indeed, the density of these precipitates and their specific properties, e.g., their sizes, compositions, and shapes have often a dramatic influence on material properties. From a more fundamental viewpoint, it is important to identify the various reaction stages, the operating mechanisms, and the resulting kinetics.

In this paper we concentrate on the late stages of the reaction during which precipitates coarsen. When coarsening takes place by evaporation of single solute atoms from clusters and condensation of these atoms onto other clusters, the average precipitate volume $\langle l(t)\rangle$ should display a power-law dependence $\langle l(t)\rangle \propto t^x$ with a $x=d/3$ exponent in d dimensions [the Lifshitz-Slyozov-Wagner (LSW) regime].[3,4] At low temperatures atom transport between clusters may become very slow and the coarsening of the precipitates may then take place by diffusion and coagulation of individual clusters [the Binder-Stauffer (BS) regime].[5] In that case, if cluster diffusion results from solute-atom transport along interfaces, the coarsening exponent is predicted to take the values $d/(3+d)$ and $d/(2+d)$ at low and intermediate temperatures, respectively.[5,6] It should be noticed that the asymptotic regime is always expected to be the LSW one, since cluster-diffusion coefficients tend to zero when the cluster size increases.

The above calculations however do not take into account the fact that in most crystalline alloys atom diffusion proceeds by a vacancy mechanism (e.g., see Ref. 7). Analytical modeling and atomistic computer simulations have shown recently that the actual mechanism by which atoms diffuse has in fact a strong influence on the leading coarsening mechanism: when atom diffusion proceeds by direct atom-exchange (Kawasaki dynamics) the evaporation condensation should be predominant, even at low temperatures, whereas the vacancy mechanism should favor the diffusion-coagulation mechanism at low enough temperatures.[8,9] The origin of this difference is well understood: it is due to the fact that at low temperatures, vacancies are not distributed homogeneously in the solid, which then results in an enhanced mobility at the precipitate-matrix interfaces.

This enhanced mobility at interfaces is however a very particular situation as we will show in this work. Indeed, the kinetic Ising models used by Fratzl and Penrose[8] and by Rautiainen and Sutton[9] present many symmetrical properties that are not likely to be observed in real alloys, e.g., in the two pure phases, vacancy presents the same formation energy and the same migration energy and isolated solute atom mobilities are equal. In the framework of the kinetic Ising-like model, a difference in homoatomic bond energies makes it possible to account for the asymmetry of atomic mobilities. This asymmetry parameter can be defined as $a^* = (\epsilon_{AA}-\epsilon_{BB})/(\epsilon_{AA}+\epsilon_{BB}-2\epsilon_{AB})$, where ϵ_{ij} is the energy associated with an i-j pair of atoms. In the above mentioned works a^* was set to zero. However when this parameter is allowed to vary, this results in an asymmetry of both vacancy

formation and migration energies (without affecting the equilibrium phase diagram). We show in this paper that it changes many aspects of the coarsening kinetics. For many metallic alloy systems, the absolute value of this reduced asymmetry parameter is larger than unity,[10] which indicates that asymmetry effects are likely to be important from a practical point of view.

The effect of the asymmetry of homoatomic interactions on the kinetic path of alloys undergoing phase transformations has in fact begun to be studied a few years ago, but mostly in the context of ordering reactions.[11–15] More recently, in the case of a binary alloy undergoing phase separation on a body-centered-cubic lattice, Athènes *et al.*[16] have shown that the asymmetry parameter has a strong influence on the mobility of small solute-atom clusters (monomers, dimers, trimers, etc.). This affects the precipitation kinetics both during the nucleation stage[16,17] and during the coarsening stage.[16] The results obtained for these small clusters indicate that, at a given annealing temperature, a positive asymmetry parameter favors the diffusion-coagulation mechanism, while a negative asymmetry parameter favors the evaporation-condensation mechanism. In this present work we will confirm directly this rationalization by analyzing the evolution of the whole cluster distribution. In addition we will show how the precipitate composition and morphology are also controlled by the asymmetry parameter.

The paper is organized as follows. The atomistic diffusion model and the kinetic Monte Carlo algorithm are presented in Sec. II. In Sec. III we successively study the effect of the asymmetry parameter on the vacancy segregation (Sec. III A), on the precipitation kinetics (Sec. III B), and on the precipitate composition and morphology (Sec. III C). As an application of the results presented in the paper we will consider (Sec. IV) the recent experimental observations on the morphology of Co precipitates in a Cu matrix obtained using a three-dimensional atom probe.[18] In Sec. V, a summary of results is given.

II. ATOMISTIC KINETIC MODEL

Since the basis of the kinetic model has been described in several articles,[11,19] only a brief summary will be given here.

Energetics. We consider an *A*-*B* binary alloy with a highly diluted vacancy *V* concentration on a rigid lattice with a face-centered-cubic (fcc) structure. To describe the chemical ordering processes, the energetics is based on an Ising-like model that depends on two terms. (i) $\epsilon=\epsilon_{AA}+\epsilon_{BB}-2\epsilon_{AB}$, which is an effective pair interaction between atoms. For fcc structures, it is small beyond first neighbors[20] and we restrict ourselves to first nearest-neighbor interactions here. ϵ is directly related to the bulk phase diagram of the system considered. Its sign gives the tendency towards ordering ($\epsilon>0$) or towards phase separation ($\epsilon<0$). (ii) $u=\epsilon_{AA}-\epsilon_{BB}$, which accounts for the difference in vacancy formation energies in the two elements. The system being highly diluted with respect to vacancies, u does not affect the equilibrium phase diagram. Its sign gives the tendency of the vacancy to occupy *A*-rich regions ($u>0$) or *B*-rich regions ($u<0$).

Kinetics. The diffusion occurs via vacancy *V* jumps towards nearest-neighbor *X* atoms, where *X* equals *A* or *B*. The activation energy E_{VX}^{act} for these jumps is derived from the broken-bond model previously described in Refs. 11, 19, and 21, and corresponds to the energy required to move a *X* atom from its initial stable site to the *XV* saddle point. Notice that in this model the contribution of the jumping atom to the saddle point configuration energy is taken as a constant. The activation energy reads

$$E_{VX}^{\mathrm{act}}=\begin{cases} E^0-\frac{1}{2}n_A(1+a^*)\epsilon & \text{if } X=A \\ E^0-\frac{1}{2}n_B(1-a^*)\epsilon & \text{if } X=B, \end{cases} \tag{1}$$

where E^0 is the configuration independent term, $a^*=u/\epsilon$ is the degree of asymmetry, n_A and n_B are the number of *A* and *B* nearest neighbors of the atom *X* to be exchanged with the vacancy *V*. In order to simplify comparisons, E^0 is kept constant when a^* is varied. Atom-vacancy exchange frequencies are calculated using rate theory.

Microscopic parameters. In this work, we focus on alloys that present a tendency to bulk phase separation. The effective pair interaction ϵ is set to -55.3 meV in order to reproduce a moderate positive heat of mixing, typical of the Cu-Co system, with a critical temperature of the miscibility gap, $T_c\approx 0.8162Z\epsilon/4k\approx 1572$ K,[22] where *Z* is the number of first neighbor atoms (12 in the fcc structure). The values of the kinetic parameters are $E^0=585$ meV and an attempt frequency $\nu=10^{-14}\ \mathrm{s}^{-1}$ (these terms only affect the time scale by a constant factor).

Concerning the atomic mobility in the two pure phases, we want to stress that the asymmetry parameter a^* controls both the difference in vacancy-formation energies ΔE^{f} and the difference in vacancy-migration energies ΔE^{m}. Indeed, it is easy to show that within the present model $\Delta E^{\mathrm{m}}=2\Delta E^{\mathrm{f}}=-Za^*\epsilon$. For fcc metals, these quantities ΔE^{f} and ΔE^{m} are also related since they both roughly scale with the difference in melting temperatures. A compilation of the available experimental data shows that, on average, the present model overestimates ΔE^{m} by a factor of 4 for a given ΔE^{f}.[23] We also notice that some systems display significant deviations with respect to this average behavior. To fit ΔE^{m} for a specific alloy system, a second asymmetry term can be added in the activation energies.[19] In this work, however, our objective is to study generic effects and the present model, despite its limitations, is therefore appropriate. Finally, let us mention that a^* also affects impurity diffusion: the *A* impurity diffusion coefficient, normalized by the vacancy concentration, is larger than the *B* impurity diffusion coefficient when $a^*>0$.[16]

Monte Carlo simulations. In conjunction with this kinetic atomistic model, Monte Carlo simulations of the kinetic process are performed by using the residence-time algorithm.[19,12] This algorithm is equivalent to the *n*-fold way algorithm.[12,24,25] The simulation box contains $(L_b\times L_b\times L_b)$ sites in the fcc structure with periodic boundary conditions with $L_b=32,64,128$. The initial condition consists of a disordered alloy with N_A *A* majority atoms, N_B *B* minority atoms and one vacancy *V*, corresponding to a vacancy con-

centration of 3.05×10^{-5}–4.77×10^{-7}. To compare results obtained with different box sizes, simulation time is rescaled to give kinetics with an apparent vacancy concentration of 4.77×10^{-7}. The system presents an initial homogeneous concentration $c=5\%$ of B atoms and is quenched at a low temperature $T=0.258T_c$.

Average precipitate size. To study the precipitation kinetics in the simulations, the average cluster size $L(t)$ is monitored. As possible definitions of $L(t)$ we use

$$L^{(1)}(t)=\sum_{l=l_c}^{\infty} l n_l(t) \Big/ \sum_{l=l_c}^{\infty} n_l(t) \tag{2}$$

$$L^{(2)}(t)=\sum_{l=l_c}^{\infty} l^2 n_l(t) \Big/ \sum_{l=l_c}^{\infty} l n_l(t). \tag{3}$$

$n_l(t)$ denotes the number of clusters that contain l B atoms, and where any two first-neighbor B atoms are said to belong to the same cluster. Following the criterion given in Ref. 26 the cutoff l_c in Eq. (2) is chosen such that the thermal equilibrium cluster numbers n_l^{eq} at the miscibility gap satisfy the condition

$$\sum_{l=l_c}^{\infty} n_l^{\mathrm{eq}} \ll \sum_{l=l_c}^{\infty} n_l(t) \tag{4}$$

for the times of interest. In this sense, we have used $l_c=5$ atoms for $T\approx0.25T_c$. In this work, we have computed both volumes [Eqs. (2) and (3)] but we only report the $L^{(1)}(t)$ behavior (unless specified otherwise), since both quantities are very similar.

III. RESULTS AND ANALYSIS

A. Equilibrium-vacancy concentration for a precipitate/matrix system

Our goal in this section is to determine quantitatively the interdependence between a^* and the local vacancy distribution in an alloy containing coherent precipitates. For this purpose we derive a simple mean-field model and we apply it to typical configurations produced by our low-temperature Monte Carlo simulations, i.e., a matrix containing nearly pure precipitates containing 10 to 1000 atoms.

Consider an A-B solid solution consisting of N fcc sites occupied by $N(1-c)$ majority A atoms, Nc minority B atoms and a highly diluted number of vacancies Nc_v ($c_v \ll c$). When coarsening takes place after quenching at very low temperature, the average number of clusters n_l is $Nc/\langle l\rangle$, where $\langle l\rangle$ is the average number of B atoms per precipitate, i.e., $\langle l\rangle$ is the dimensionless average volume of the precipitates. For simplicity, we neglect cluster-size dispersion and separate the system into n_l identical blocks, each of them consisting of a spherical pure B precipitate of size $\langle l\rangle$ atoms embedded in a nearly pure A matrix containing $\langle l\rangle(1-c)/c$ atoms [Fig. 1(a)]. Taking advantage of the spherical symmetry of the configuration, let us decompose the volume into atomic concentric shells, centered on the precipitate and distinguish four different regions: (1) the shells of B atoms having only B first neighbors (precipitate core), (2) the shell of B atoms having both A and B first neighbors (internal interface), (3) the shell of A atoms having both A and B first neighbors (external interface), and (4) the shells of A atoms having only A first neighbors (matrix). For a given chemical configuration, the local vacancy concentration at equilibrium is in general different in these four regions. We thus define c_v^- and c_v^+ as the vacancy concentrations at the immediate vicinity of the interface, in the internal and external interface shells, respectively, and c_v^A and c_v^B as the vacancy concentrations in the matrix and in the core of the precipitate, respectively [Fig. 1(b)]. The average number of vacancies per block is $Nc_v/n_l=\langle l\rangle c_v/c$ and can be written as a sum of vacancy numbers over the four considered regions in the block,

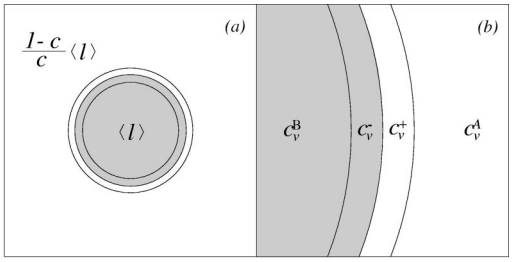

FIG. 1. Schematic representation of a block. The left sketch (a) represents a pure B precipitate of size $\langle l\rangle$ atoms embedded in a pure A matrix containing $\langle l\rangle(1-c)/c$ atoms. The right sketch (b) shows the four distinct regions where the local vacancy concentrations c_v^i may differ.

$$\langle l\rangle\frac{c_v}{c}=\left[\langle l\rangle\frac{1-c}{c}-(\langle l^+\rangle-\langle l\rangle)\right]c_v^A+[\langle l^+\rangle-\langle l\rangle]c_v^+ +[\langle l\rangle-\langle l^-\rangle]c_v^-+\langle l^-\rangle c_v^B, \tag{5}$$

where the dimensionless volumes $\langle l^+\rangle$ and $\langle l^-\rangle$ are defined in such a way that $\langle l^+\rangle-\langle l\rangle$ and $\langle l\rangle-\langle l^-\rangle$ are the numbers of sites in the external and internal interface shells, respectively.

In addition to the conservation equation (5), one can determine relations between local vacancy concentrations by assuming that the vacancy distributions are at local equilibrium in the block. This assumes that vacancies reach equilibrium with a characteristic time scale much smaller than that for the evolution of the average precipitate size. The simplest approximation is to express vacancy concentrations as depending only on a segregationlike energy per inequivalent site, that is, the energy needed to exchange an atom in a given site with a vacancy from the A block side.[27] Segregation equilibrium equations for dilute vacancy concentrations read

$$c_v^+\approx c_v^A\exp\left\{-\frac{Z^-(1+a^*)\epsilon}{2kT}\right\}, \tag{6}$$

$$c_v^-\approx c_v^A\exp\left\{-\frac{[Z^+(1-a^*)+2Za^*]\epsilon}{2kT}\right\}, \tag{7}$$

$$c_v^B \approx c_v^A \exp\left\{-\frac{Za^*\epsilon}{kT}\right\}, \tag{8}$$

where Z^- and Z^+ are the numbers of B and A neighbor atoms, respectively, of a site located in the external and internal interface shells, respectively.

The partial coordination numbers Z^- and Z^+ are a function of the precipitate size. To calculate this dependency, we use a cubo-octahedron geometry that is known to be one of the more stable cluster shapes in the fcc structure and for which all the parameters in Eq. (5) can be defined (see Appendix A).[28]

In addition to Eqs. (5)–(8), one more equation is required to fully determine the five vacancy concentrations that we have introduced. In the kinetic simulations presented in the following sections as well as in nearly all atomistic kinetic simulations published so far on second-phase precipitation, it has been assumed that the total vacancy concentration is fixed (i.e., treating vacancies as conservative species), thus providing the required fifth equation. This approximation is valid if one assumes that the excess of vacancies right after quenching is eliminated well before any significant modification of the composition field, and that the equilibrium vacancy concentration is independent or only weakly dependent on the microstructure of the alloy. Since here we do not concentrate on the early stages of precipitation, it is reasonable to assume that the above assumptions are valid.

From Eqs. (6)–(8) we can now study the influence of the asymmetry parameter a^* on the vacancy distribution. For different values of a^*, we plot the local vacancy concentrations as a function of $\langle l\rangle$ (Fig. 2) and the total number of vacancies in the precipitate $N_v^l=[\langle l\rangle-\langle l^-\rangle]c_v^-+\langle l^-\rangle c_v^B$ [Fig. 3(a)]. For two typical $\langle l\rangle$ values (20 and 200), we also plot [in Fig. 3(b)] the probabilities to find the vacancy in each region, P_v^A, P_v^+, P_v^-, and P_v^B, obtained from Eq. (5). The temperature T and the concentration c correspond to the ones taken in the following sections for the Monte Carlo simulations, i.e., $T=0.258T_c$ and $c=0.05$.

(i) Standard case ($a^*=0$). When A and B pure phases present the same vacancy formation energies, the matrix and the precipitate contain the same vacancy concentration, $c_v^B \approx c_v^A$. Vacancies tend to segregate at the interface to minimize the number of heteroatomic bonds and when the precipitate size decreases, vacancies are preferentially located in the internal interface shell since the number of AB bonds is greater there. In Fig. 2(b), we indeed observe that $c_v^- > c_v^+ \gg c_v^B, c_v^A$. Furthermore, we note that c_v^- varies very slowly for $\langle l\rangle < 1000$ atoms. As a consequence, we obtain numerically in Fig. 3 that the total number of vacancies in the precipitate, N_v^l, is proportional to the number of sites in the internal interface shell and can be written as

$$N_v^l \approx \frac{c_v}{c}[\langle l\rangle-\langle l^-\rangle]. \tag{9}$$

(ii) For negative values of a^* the vacancy-formation energy is smaller in the A phase than in the B one and thus $c_v^A > c_v^B$. In Fig. 2(c) the case $a^*=-0.5$ is shown at $T=0.258T_c$. As expected, we observe that vacancies are rarely found in the precipitate and that $c_v^+, c_v^A \gg c_v^-, c_v^B$. When $a^* \leqslant -1$, vacancy depletion occurs both in the precipitate and at the interface, $c_v^+ \leqslant c_v^A$, since breaking AB bonds becomes energetically less favorable than breaking AA bonds. Regarding the cluster size effect for $a^* \leqslant -0.5$, the vacancy depletion in the precipitate is less pronounced for small precipitate and controls the $\langle l\rangle$ dependence of the total number of vacancy per precipitate. By keeping only the significant c_v^A term in Eq. (5) and combining with Eq. (7), we find

$$N_v^l \approx \frac{c_v}{1-c}[\langle l\rangle-\langle l^-\rangle]\exp\left\{-\frac{[Z^+(1-a^*)+2Za^*]\epsilon}{2kT}\right\}. \tag{10}$$

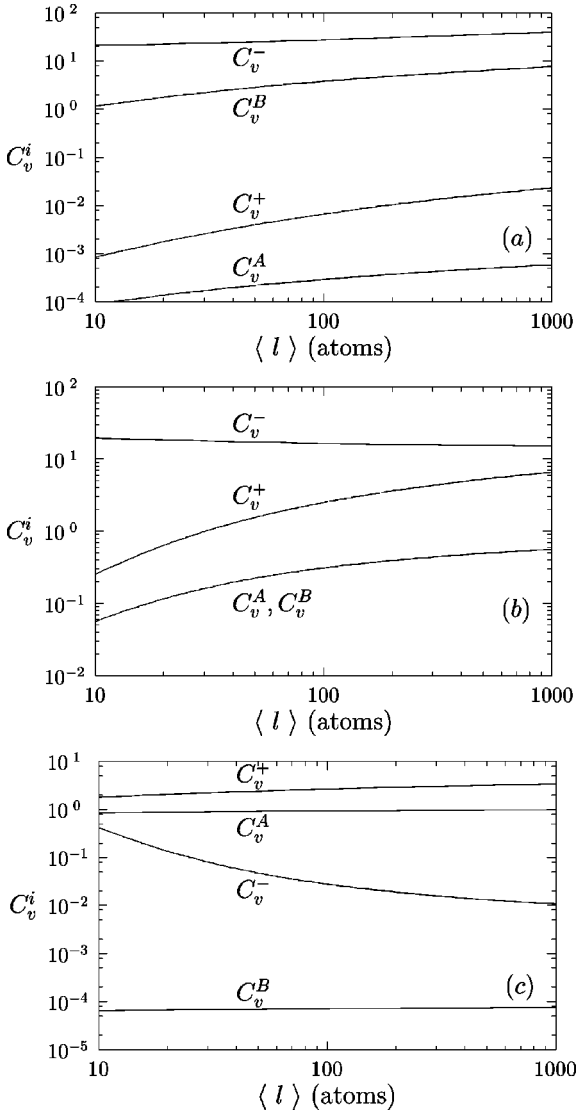

FIG. 2. Equilibrium local vacancy concentrations C_v^i in a block as a function of average size precipitate $\langle l\rangle$ for: (a) $a^*=0.5$, (b) $a^*=0$, and (c) $a^*=-0.5$ at $T=0.258T_c$ and with $c=0.05$. C_v^i concentrations are scaled to the nominal concentration c_v ($C_v^i=c_v^i/c_v$).

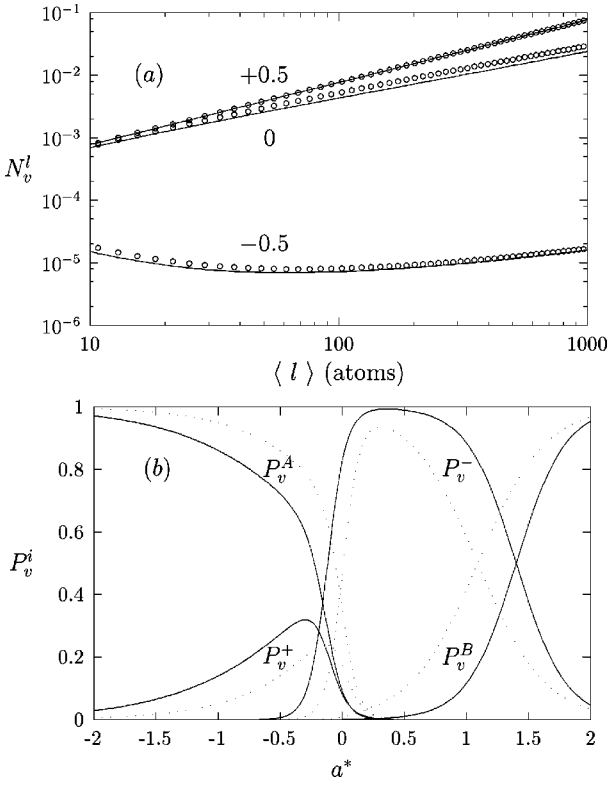

FIG. 3. (a) Mean number of vacancies N_v^l into one precipitate against average-size precipitate $\langle l \rangle$ (solid lines) for $a^*=+0.5$, 0, -0.5 at $T=0.258T_c$ and with $c=0.05$. Approximations formulated in Eqs. (9)–(11) are also reported (○). (b) Probabilities to find the vacancy in each region P_v^A, P_v^+, P_v^-, and P_v^B for $\langle l \rangle = 20$ atoms (solid lines) and 200 atoms (dotted lines).

Figure 3 shows that for $a^*=-0.5$ the exponential term in Eq. (10) becomes dominant at the temperature considered, leading even to a decrease of N_v^l with $\langle l \rangle$ for $\langle l \rangle < 100$ atoms.

(iii) For positive values of a^* [Fig. 2(a)] vacancies are now trapped into the cluster and, when $a^* \geqslant 1$, mostly in the core precipitate shells. N_v^l exhibits a different precipitate size dependence, proportional to $\langle l \rangle$ (see Fig. 3), which from Eq. (5) can be written as

$$N_v^l \approx \frac{c_v}{c}\langle l \rangle. \tag{11}$$

We have shown in this section that the local equilibrium vacancy concentration for a precipitate/matrix system depends strongly on the asymmetry term a^*. We will now see that this results in major changes in the precipitation kinetics.

B. Growth and coarsening of the precipitates

1. Kinetic Monte Carlo results

By performing Monte Carlo simulations with the kinetic atomistic model described in Sec. II, we study the kinetics of phase separation of a $A_{95}B_5$ random alloy after a deep quench from an infinite temperature to a temperature well into the miscibility gap at $T=0.258T_c$. This low temperature has been chosen so as to enhance the differences produced

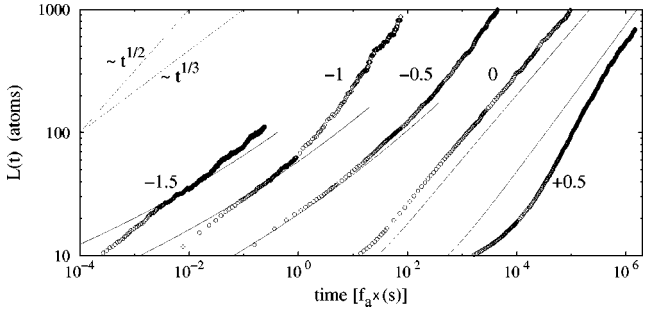

FIG. 4. Monte Carlo time evolution of the average cluster volume $L(t)$ (○) at $T=0.258T_c$ with $c=0.05$, $c_v=4.77\times10^{-7}$, and for various a^* values ($a^*=-1.5,-1,-0.5,0,0.5$). Simulation boxes contain 128^3 fcc sites except for $a^*=-1.5,-1$ (64^3 fcc sites only). For the sake of clarity, the Monte Carlo time is scaled by a factor f_{a^*}: $f_{-1.5}=4\times10^4$, $f_{-1}=8\times10^2$, $f_{-0.5}=10$, $f_0=8$, and $f_{0.5}=1$. Solid lines represent predictions of the coagulation model (see text).

by varying a^*. The composition has been chosen so as to start with a very large supersaturation (the solubility limit c_α at this temperature is 7.6×10^{-5}) in order to focus on the growth and coarsening regimes and also to increase the statistics on precipitate properties. In Fig. 4, we report on a log-log plot the time evolution of the mean cluster size $L(t)$ as defined in Sec. II for different values of the asymmetry parameter a^*. Estimation of the exponents $x = d\{\ln[L(t)]\}/d[\ln(t)]$ are summarized in Table I. In this work we do not attempt to measure accurately the coarsening exponents (this task can be quite difficult[29,30]). The variations of x with a^* are, however, large enough so that our simple estimation is sufficient for our purpose.

Let us first consider the standard case ($a^*=0$). Figure 4 shows that the mean volume $L(t)$ increases with time according to a $L(t)\propto t^x$ law with an exponent $x\approx0.52$ for a large range of $L(t)$ [$10<L(t)<1000$]. When we introduce some asymmetry we measure different exponent values x. At short times [$L(t)<100$ atoms] for negative a^* values, a smaller exponent x is measured, $x\approx0.33$ for $a^*=-0.5$ and $x\approx0.34$ for $a^*=-1,-1.5$. At long times [for $100<L(t)<1000$ atoms], the exponent x depends on the value of a^* considered: for $a^*=-0.5$, x increases continuously up to a

TABLE I. Coarsening exponents x of the average precipitate volume [$L(t)\propto t^x$], obtained from the kinetic Monte Carlo simulations and from our coagulation model (in Fig. 4), for the various a^* values considered. Letters (c) for cluster coagulation-diffusion and (e) for solute evaporation-condensation indicate which coarsening mechanisms are present.

a^*	Short times [$L(t)<100$]	Long times [$L(t)<1000$]	Coagulation model
+0.5	0.80 (c)	0.62 (c)	0.60 (c)
0	0.52 (c)	0.52 (c)	0.52 (c)
−0.5	0.33 (c+e)	> 0.50 (e)	0.33 (c)
−1.0	0.34 (c+e)	0.63 (e)	0.27 (c)
−1.5	0.34 (c+e)	NA	0.23 (c)

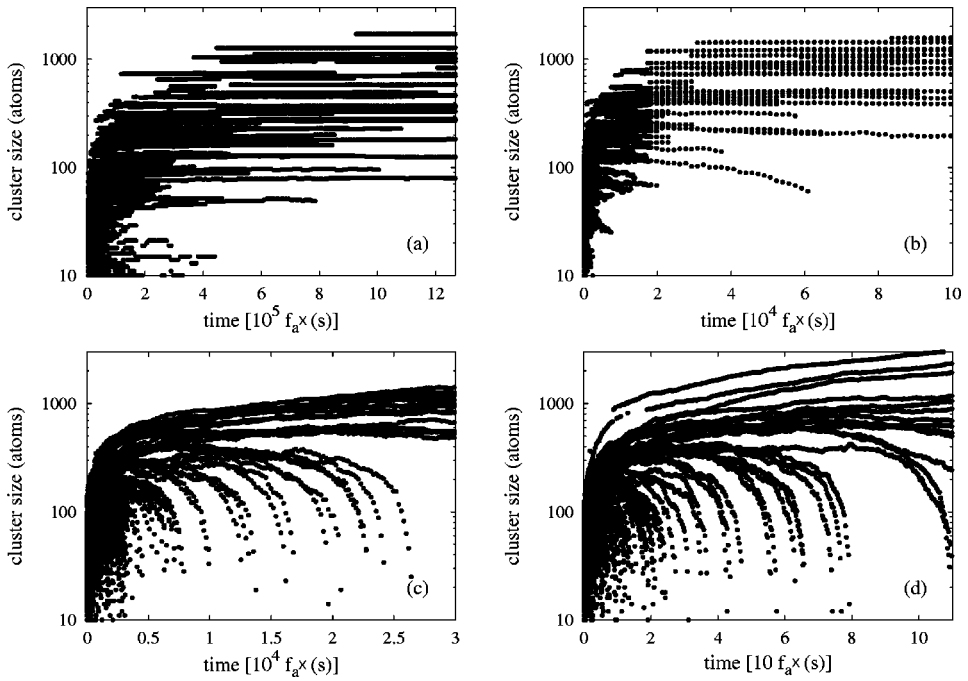

FIG. 5. Illustration at late stages of the *stairlike* (a),(b) and the *fountainlike* (c),(d) evolutions obtained by plotting Monte Carlo time variations of all cluster sizes (●) at $T=0.258T_c$ with $c=0.05$ and for various a^* values: (a) $a^*=0.5$, (b) $a^*=0$, (c) $a^*=-0.5$, (d) $a^*=-1$. Simulation boxes contain 64^3 fcc sites and scaling factors f_{a^*} are taken from Fig. 4.

value greater than 0.5; for $a^*=-1$, x exhibits a value close to 0.63; while for $a^*=-1.5$ the kinetics becomes very slow and limitations in computing times prevent us from exploring $L(t)$ values greater than 110 atoms. Finally for $a^*=0.5$, a much larger exponent, $x\approx 0.80$, is found for $30<L(t)<400$ atoms, which decreases to approach a value close to $x\approx 0.62$ for $400<L(t)<700$. Notice that in this latter case, $L^{(2)}(t)$ differs slightly from $L(t)$ by approaching the lower exponent $x\approx 0.62$ faster [when $L(t)=100$].

To determine the extension of the nucleation and growth regimes, we have calculated the evolution of the number of precipitates larger than l_c. It starts to decrease as soon as $L(t)>10$ atoms for the considered values of $a^*\leqslant 0$ and when $L(t)>15$ atoms for $a^*=0.5$. Consequently, the measured exponents x correspond mostly to coarsening regimes.

To identify the mechanisms responsible for coarsening, we introduce a graphical method that is illustrated at long times in Fig. 5. It consists in reporting on a same graph the size evolution of all precipitates. For a simulation box such that the cluster number is low (typically below 100), it is then possible to directly visualize the precipitate kinetics behavior. From Fig. 5, depending on the a^* values, one can distinguish two very different behaviors: a *stairlike* evolution for $a^*=0,0.5$ and a *fountainlike* evolution for $a^*=-0.5$, $-1,-1.5$.

(i) the stairlike behavior [Figs. 5(a) and 5(b)] is a clear signature of a coarsening regime by diffusion and coagulation of the clusters. Indeed, it consists of a distribution of horizontal segments, each of them corresponding to at least one precipitate. When one precipitate of size l_1 disappears (right end of one segment), another of size l_2 does too at the same time and a new precipitate of size l_1+l_2 is formed (left end of one segment).

(ii) The fountainlike behavior [Figs. 5(c) and 5(d)] demonstrates the presence of a coarsening regime occurring by evaporation and condensation of solute atoms from small precipitates to larger ones (Ostwald ripening). One can indeed clearly observe two types of precipitates, the smaller ones, which decrease rapidly in size and are dissolved and the larger ones, which grow continuously.

At long times, we therefore recover the two well-known coarsening mechanisms. We show here that the exponents $x\approx 0.52$ and $x\approx 0.80,0.62$ obtained, respectively, for $a^*=0$ and $a^*=0.5$ correspond to a cluster diffusion and coagulation regime. On the other hand, the exponent $x\approx 0.63$ measured for $a^*=-1$ is due to Ostwald ripening.

At short times, it is convenient to use smaller simulation cells in order to distinguish the different trajectories corresponding to each cluster. By using 32^3 site cells, we also recover pure coagulation regime for $a^*=0$ and $a^*=0.5$. For $a^*=-0.5$, the situation differs from the one at long times. For $L\approx 50$ atoms, we now observe some coagulation events that roughly concern half of the cluster population that disappears. This therefore suggests that the very small exponent $x\approx 0.33$ obtained during this stage is partly controlled by the coagulation regime. For $a^*=-1$ and $a^*=-1.5$, coagulation events are also identified at short times. However, they become rapidly very rare as soon as $L>50$ atoms.

2. Analysis

Previous theoretical models of the kinetics of phase separation have predicted some of the power-law exponents x that we measure in this work. According to the LSW theory,[3,4] the coarsening via evaporation and condensation of single solute atoms is predicted to exhibit $x=1$ at late stages. The Langer–Bar-On–Miller theory,[31,2] which is valid even when the Gibbs-Thomson relation cannot be linearized, however yields $x\approx 0.63$ at earlier stages of coarsening. This value agrees very well with the one obtained in our simulations for $a^*=-1$.

On the basis of their cluster-diffusion-coagulation model (without vacancy), Binder and Stauffer[5] predict $x=0.5$ and

$x=0.6$ for low and intermediate temperatures, respectively. This also compares well with our simulations performed at low temperature (at $T\approx 0.25T_c$) for $a^*=0$ where we measure a coagulation exponent $x\approx 0.52$. Recent two-dimensional (2D) Monte Carlo simulations with a vacancy-mediated diffusion mechanism and for $a^*=0$ also agree with the BS theory. In particular, Fratzl and Penrose[8] show that at intermediate temperature the Brownian cluster diffusivity should lead to a coagulation exponent $x=0.6$. In a recent exhaustive work, Rautiainen and Sutton[9] also reported similar results at $T=0.5T_c$.

These theoretical predictions, however, do not explain all the power-law exponents obtained in our simulations. This is particularly true for the low coagulation exponent ($x\approx 0.33$) obtained for $a^*=-0.5$ and for the high coagulation exponents ($x\approx 0.80,0.62$) found for $a^*=0.5$. To understand why x increases with a^*, we propose to estimate the coagulation exponents x from our vacancy mean-field model developed in Sec. III A. Cluster Brownian-diffusion coefficients are calculated from the Einstein formula. For a cluster of size $\langle l\rangle$ making jumps of length Δx at time intervals Δt, its diffusivity $D_{\langle l\rangle}$ is

$$D_{\langle l\rangle}=\frac{\Delta x^2}{2d\Delta t}, \tag{12}$$

where d is the system dimensionality (3 here) and Δt is the average time for one atom of the precipitate to jump. After this jump the cluster center of gravity moves by a distance $\Delta x=1/\langle l\rangle$.[5]

The main difficulty here consists in estimating the frequency $1/\Delta t$ that results from the complex kinetic path that makes the vacancy move cluster atoms. To simplify the problem, Fratzl and Penrose[8] proposed to write $1/\Delta t\propto$ [the number of vacancies in the cluster (N_v^l)]$\times$[the vacancy jump frequency in the cluster]$\times$[the vacancy probability to cross the interface]. At intermediate temperature, assuming $N_v^l\propto\langle l\rangle$, these authors obtained $D_{\langle l\rangle}\propto\langle l\rangle^{-1}$ and the resulting coagulation exponent $x=0.6$ as predicted by the BS theory.

In this work, we improve this approach by explicitly taking into account the fact that vacancy distribution is not uniform at low temperature and is strongly influenced by a^* (see Sec. III A). Using Eqs. (9)–(12), and first neglecting the possible contributions coming from jump frequencies, we now calculate the $\langle l\rangle$ dependency of $D_{\langle l\rangle}$. For $a^*=0.5$, $N_v^l\propto\langle l\rangle$ (cluster volume) and thus $D_{\langle l\rangle}$ exhibits the high-temperature $\langle l\rangle$ dependence, i.e., $\propto\langle l\rangle^{-1}$. For $a^*=0$, $N_v^l\propto\langle l\rangle^{2/3}$ (cluster surface) and $D_{\langle l\rangle}$ decreases faster with $\langle l\rangle$, i.e., $\propto\langle l\rangle^{-4/3}$. Finally, for $a^*=-0.5$, N_v^l varies very slowly and even can decrease with $\langle l\rangle$ [see Fig. 3]. This leads to a very fast decrease of $D_{\langle l\rangle}$ with $\langle l\rangle$ (i.e., $\propto\langle l\rangle^{-y}$ where $y>2$ for $\langle l\rangle<100$).

Following Binder and Stauffer[5] and Fratzl and Penrose,[8] the coagulation rate is given by $d\langle l\rangle/dt\propto D_{\langle l\rangle}c^{2/d}\langle l\rangle^{1-2/d}$. Replacing in this formula the above $D_{\langle l\rangle}$ expressions, we plot in Fig. 4 the predicted time evolution for $\langle l\rangle$, which we compare with the kinetic Monte Carlo results (see also Table I).

Qualitatively our model reproduces the new result that the coagulation exponent x increases when a^* increases. For $a^*=0.5$, the coagulation model gives $x=0.60$ as observed at late stages in the simulations ($x\approx 0.62$) but does not predict the large exponent $x\approx 0.80$ found at short times. The maximum value $x\approx 0.60$ that the model can predict shows the limitations of the present description. In the model, all precipitates are assumed to have the same size, which is not the case in the simulations for $a^*=0.5$ where the cluster-size distribution presents, at short times, a large contribution from the small precipitates. This explains why, as already mentioned, $L^{(2)}(t)$ differs from $L(t)$ in this case and approaches faster the predicted exponent $x\approx 0.62$. (Remember that $L^{(2)}(t)$ [in Eq. (3)] is dominated by large cluster sizes.) For $a^*=0$, both model and simulations agree with the BS theory exponent $x=0.5$. For $a^*=-0.5$ both our simulations and our coagulation model yield the same low exponent $x\approx 0.33$ at the early stage of the coarsening. Finally, for $a^*=-1,-1.5$ the coagulation model does not apply since coagulation is no longer the dominant mechanism for coarsening (see Sec. III B 1). It is therefore not surprising that the predicted exponents are smaller than the ones measured in the simulations.

Notice also that one of the model assumptions is to use the same frequency for any vacancy jump in the precipitate. At the interface vicinity this frequency is however highly anisotropic and therefore should modify the average frequency (noted $1/\Delta t$) corresponding to a typical cluster-atom jump. Moreover, correlated jumps take place at low temperature and should also affect $1/\Delta t$. For instance, recent kinetic Monte Carlo simulations performed by Rautiainen and Sutton[9] for $a^*=0$ and at a very low temperature $T\approx 0.16T_c$ have put in evidence, a coagulation exponent $x\approx 0.21$ well below the expected $x\approx 0.5$ for this symmetric case. Preliminary extensions of our model, where these correlated jumps are taken into account indicate that x decreases significantly when the annealing temperature is lowered.[32]

C. Microstructure of the precipitates

1. Kinetic Monte Carlo results

Cluster and matrix composition. From the kinetic Monte Carlo simulations presented in the previous section we now investigate the influence of the asymmetry term a^* on the cluster composition. We calculate three different concentrations: c_B^A, the concentration of B atoms in the A matrix including small B clusters of size below l_c atoms; c_A^B, the concentration of A atoms in the B precipitates, including the A dimers, trimers, etc., not connected to the matrix; and finally $c_A^{B^*}$, which includes both A atoms counted in c_A^B and A atoms bonded to one or two matrix A atoms, i.e., A atoms located at the vicinity of the interface.

At the temperature considered $T=0.258T_c$, the solubility limit c_α is equal to 7.6×10^{-5}. However, when clusters are in local equilibrium with the matrix, the presence of curved interfaces increases the solubility of B in the A matrix, i.e., $c_B^A>c_\alpha$, and decreases that of A atoms in the B precipitates, i.e., $c_A^B<c_\alpha$. Thus c_B^A is a decreasing function of the cluster

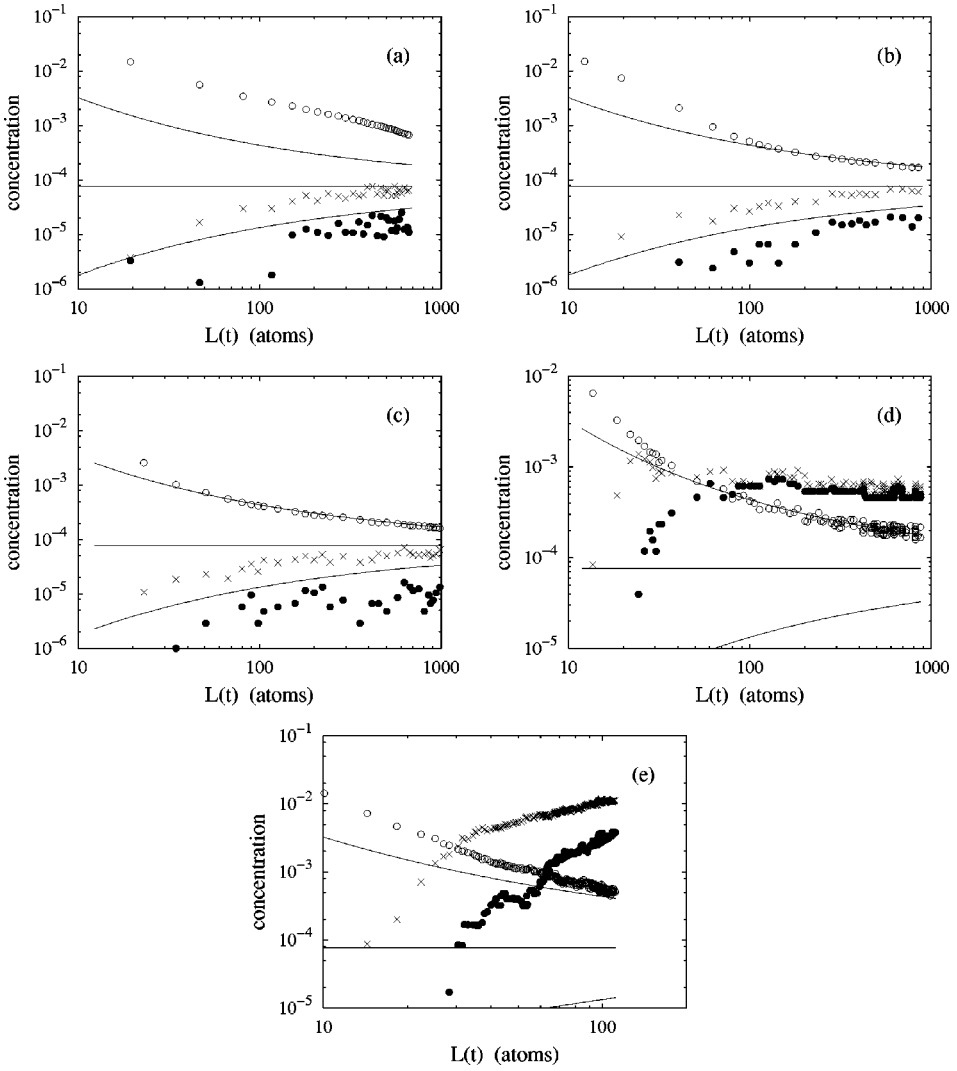

FIG. 6. Monte Carlo solubilities as a function of average cluster size $L(t)$ for: (a) $a^*=0.5$, (b) $a^*=0$, (c) $a^*=-0.5$, (d) $a^*=-1$, and (e) $a^*=-1.5$ at $T=0.258T_c$ and with $c=0.05$. c_B^A (○): concentration of B atoms in the A matrix, c_A^B (●): concentration of A atoms in the B precipitates, and c_A^{B*} (×), which includes both A atoms counted in c_A^B and A atoms bonded to one or two matrix A atoms. The horizontal solid line represents the solubility limit c_α. The two curved solid lines show the c_B^A and c_A^B Gibbs-Thomson predictions from Eq. (13) ($c_B^A > c_A^B$).

size and at low temperature obeys the following macroscopic Gibbs-Thomson law:

$$c_B^A \approx c_\alpha \exp\left\{-\frac{2\gamma\Omega}{RkT}\right\}, \tag{13}$$

where γ is the interfacial energy per unit area, Ω is the atomic volume, and R is the average precipitate radius. Conversely, $c_A^B = c_\alpha^2/c_B^A$ increases smoothly with the cluster size. Equation (13) has been tested by equilibrium Monte Carlo simulations; we obtain a very good agreement when γ is taken as the interfacial energy of the {100} orientation, i.e., $\gamma = -4\epsilon e V/a^2$, where a is the fcc lattice parameter. This is the value we have used to analyze our kinetic simulations. R is taken as the radius of a spherical precipitate of equivalent volume.

In Fig. 6 we report the evolution of the precipitate and matrix solubilities as a function of the average cluster size $L(t)$ and for the considered a^* values. We now compare the kinetic Monte Carlo (KMC) results with the equilibrium Gibbs-Thomson (GT) predictions.

Considering first the standard case ($a^*=0$) in Fig. 6(b), we observe a good agreement between KMC results and the GT relation. In the simulations, c_B^A starts from the initial solid-solution concentration $c=5\%$ and then decreases rapidly to reach the expected GT c_B^A value at $L_{GT} \approx 100$ atoms. Considering now the KMC c_A^B, although the statistic is less precise due to the very low concentration measured, we clearly observe that the average KMC c_A^B is below c_α and increases slowly with a value close to GT c_A^B.

For $a^*=-0.5$ [in Fig. 6(c)] the picture is very similar and differs only in the fact that KMC c_B^A reaches GT c_B^A for smaller precipitate size, $L_{GT} \approx 30$ atoms.

The cases $a^*=-1,-1.5$ are displayed in Figs. 6(d) and 6(e). The B concentration c_B^A becomes also close to the GT curve when $L_{GT} \approx 50$ atoms for $a^*=-1$ and $L_{GT} \approx 110$ atoms for $a^*=-1.5$. However, regarding now the A concentration in the precipitates, we observe at early stages an unexpected kinetic supersaturation of the clusters. Indeed, for $a^*=-1$, a large deviation of c_A^B is found with respect to the GT prediction, c_A^B increases rapidly and reaches at $L(t) \approx 100$ a maximum value that is two orders of magnitude larger than the GT one. Then c_A^B decreases very slowly and it is expected that it will reach the GT curve for very large $L(t)$. This kinetic-cluster supersaturation is even more pro-

TABLE II. Average precipitate sizes L_{GT} (in atom number) at which the concentration of B atoms in the A matrix, KMC c_B^A [see Fig. 6], reaches the Gibbs-Thomson prediction [Eq. (13)], at $T=0.258T_c$, with $c=0.05$ and for the various a^* values considered.

a^*	-1.5	-1	-0.5	0	0.5
L_{GT}	110	50	30	100	>700

nounced for $a^*=-1.5$. Although the kinetics becomes very slow and the maximum c_A^B value is not yet reached, at $L(t)=110$ atoms simulations reveal a supersaturation that is already greater than two orders of magnitude.

Finally, in Fig. 6(a) for $a^*=0.5$, the inverse phenomenon occurs. It is now the matrix that is kinetically supersaturated in B solute atoms. c_B^A decreases very slowly and even at $L(t)=700$ atoms remains roughly one order of magnitude larger than the GT predictions. On the other hand, clusters are almost pure and their composition c_A^B behaves as expected from the GT equation.

Concerning the above mentioned c_B^A deviations, it is interesting to notice that the characteristic size L_{GT} presents a minimum for a a^* value close to -0.5. The observed L_{GT} values are summarized in Table II and will be discussed in Sec. III C 2.

Cluster morphology. To study the influence of a^* on the cluster morphologies, we report the configuration-dependent part of the interface energy per bond in each cluster, written as

$$E_{\text{int}}=\frac{-\epsilon}{2l}\sum_i \frac{Z_i}{Z}, \tag{14}$$

where i sums over all the l B atoms of the cluster and Z_i is the number of A first neighbors of the ith B atom. This formula also includes the A atoms dissolved in the precipitates, but in all our results the total number of such A atoms is so small that this contribution is negligible. In Fig. 7, we plot the instantaneous interfacial energies of the clusters at different stages of the kinetic Monte Carlo simulations and we compare them with the interfacial energies of equilibrium regular fcc polyhedra.[28] At late stages, for $L(t)=500$ atoms and for the considered a^* values [for $a^*=-1.5$ $L(t)=500$ atoms is not available], precipitate interfacial energies are very close to cubo-octahedral and Wulff polyhedral energies, which means that precipitates adopt compact shapes and present essentially $\{111\}$ and $\{100\}$ facets with sharp interfaces. At earlier stages, $L(t)=10$, 50 atoms, the cluster-shape evolution is different and depends on a^*. When $a^*\geqslant -0.5$, the clusters present a small excess energy compared to that of equilibrium clusters. This small excess is however quite independent of the a^* values. In contrast, when $a^*\leqslant -1$, the clusters present a large excess energy, which increases when a^* decreases. For $a^*=-1.5$ some clusters carry an interfacial energy twice that of the regular polyhedra of the same volume. These large excess energies are characteristic of jagged, rough interfaces, and this is confirmed by direct visualization of the precipitates. Another remarkable feature is clearly visible in Fig. 7(e): the excess interfacial energy is larger for the larger clusters. As seen in Sec. III B this microstructure is evolving by the evaporation-condensation mechanism. We can thus identify the small clusters as the ones undergoing dissolution and the large clusters as the growing ones [see also Fig. 5(d)]. We therefore conclude that the clusters undergoing dissolution tend to have rather smooth interfaces, whereas the growing clusters develop rough interfaces.

2. Analysis

The kinetic Monte Carlo results obtained in this section with varying a^* lead us to formulate the following questions: What is the origin of the kinetic supersaturations either in the matrix or in the precipitates? What is the origin of the kinetic roughness of the growing precipitates? Concerning the first question, a partial and qualitative explanation may be found from our equilibrium vacancy model presented in Sec. III A. Indeed, the supersaturation phenomenon and the vacancy-occupation probability in the A-rich and B-rich phases are clearly correlated. When vacancies are mainly trapped into the precipitates (for $a^*\geqslant 0.5$), B atoms in the matrix diffuse very slowly towards the precipitates and therefore supersaturation persists in the matrix. Conversely, when vacancies are essentially located in the matrix (for $a^*\leqslant -0.5$), A atoms, if trapped at the precipitate internal interfaces during the growth process, will afterwards hardly diffuse and these trapped atoms will lead to supersaturated precipitates. This simple explanation, however, does not elucidate why A atoms can be trapped at growing interfaces. This trapping is also directly relevant to the development of rough interfaces. To answer these questions, both interface properties and kinetic aspects must be considered.

Let us begin by studying the transient supersaturation of the matrix and the influence of a^* on this supersaturation. The supersaturation is related to the condensation rate of B atoms at the precipitate interface. This rate is proportional to the probability of finding vacancies at the immediate vicinity of the interface on the matrix side, which exhibits a strong dependence with a^*. We therefore compare this probability, noted P_v^+ in Sec. III A and plotted in Fig. 3(b), to the L_{GT} values obtained in the simulations (see Table II), which indicate the characteristic cluster size above which kinetic matrix supersaturation has disappeared. Qualitatively, the P_v^+ curve [Fig. 3(b)] explains well the origin of the L_{GT} behavior as a function of a^*: the a^* value for which P_v^+ exhibits a maximum ($a^*=-0.3$ for $L=20$) is close to the a^* value giving the smallest L_{GT} value. In addition, the asymmetry of the L_{GT} behavior with respect to a^* is also reproduced. For $a^*<-0.5$, P_v^+ and L_{GT} vary slowly with a^* (P_v^+ decreases and L_{GT} increases), while for $a^*>0$, P_v^+ and L_{GT} exhibit marked variations with a^*. This results in a large persistent matrix supersaturation for $a^*=0.5$.

We now turn to the mechanism that yields to the supersaturation of the precipitates, i.e., the mechanism for the trapping of A solvent atoms in growing B precipitates. The direct visualization of the configurations allows us to have a first phenomenological understanding of this mechanism. In Fig. 8 we report for $a^*=-1$ a sequence of snapshots in a

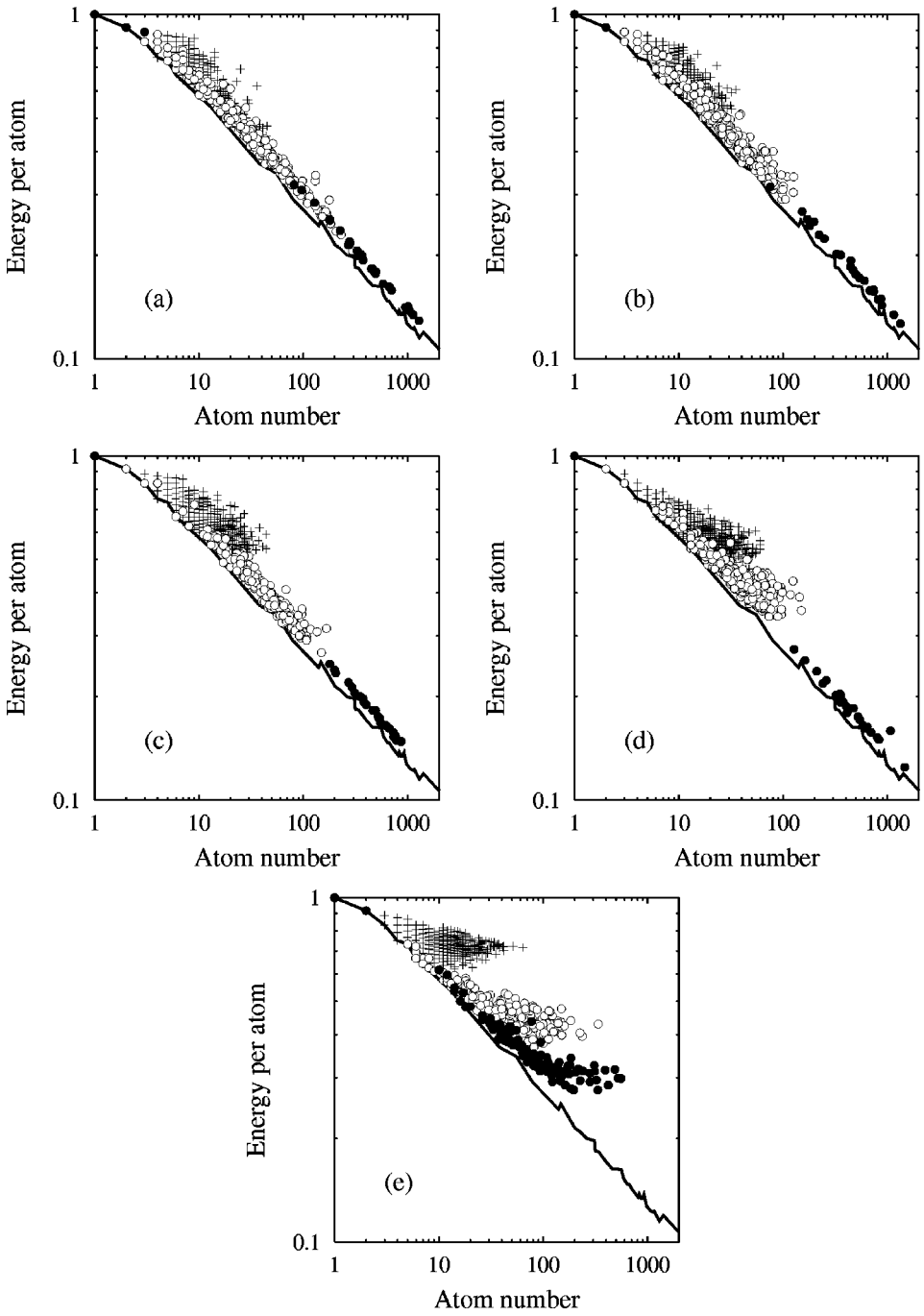

FIG. 7. Instantaneous interfacial energies per bond in each B cluster at different stages of the kinetic Monte Carlo simulations for $L(t)=10$ (+), $L(t)=50$ (○), and $L(t)=500$ (●) atoms, compared to interfacial energies of equilibrium regular fcc polyhedra (solid lines): (a) $a^*=0.5$, (b) $a^*=0$, (c) $a^*=-0.5$, (d) $a^*=-1$, (e) $a^*=-1.5$ [here, (●) points correspond to $L(t)=100$]. Energies are calculated from Eq. (14).

{111} plane taken from a 3D 64^3 simulation box. This reveals a typical incorporation process of one A solvent atom: The A atom is first trapped on the internal side of the interface and is covered by incoming B atoms later on. This observation is in agreement with the sequential increases measured for the solubilities c_A^{B*} and c_A^B [Figs. 6(d) and 6e)]. It should be noticed that the number of trapped A solvent atoms responsible for the supersaturation measured in Fig. 6 is in fact very small and in the range of 10 atoms for a 64^3 cell with $c=5\%$ at $T\approx 0.25T_c$ and $a^*=-1$. Thus, the presence of one trapped A atom that persists during the kinetics shown in Fig. 8 is representative of the supersaturation. By following the kinetic behavior of these trapped A atoms, we can draw two important conclusions. The supersaturation buildup is associated with the presence of some interface roughness [Figs. 8(a) and 8(b)], which is consistent with our interfacial-energy calculations [Fig. 7]. The release into the matrix of a trapped A atom occurs by the complete dissolution of the precipitate that contains it [Figs. 8(c)–8(f)]. Qualitatively, this is in agreement with the fact (shown in Sec. III A) that for $a^*\leqslant -1$ the vacancy rarely visits the inside of the clusters and therefore does not let A atoms escape from them.

Having now a qualitative picture of the supersaturation mechanism, one can wonder why the trapping mechanism occurs easily for $a^*\leqslant -1$ and does not happen for $a^*\geqslant -0.5$. To elucidate this problem we start from our observation that the A atoms trapped at cluster interfaces are then covered and trapped inside the clusters by the arrival of B

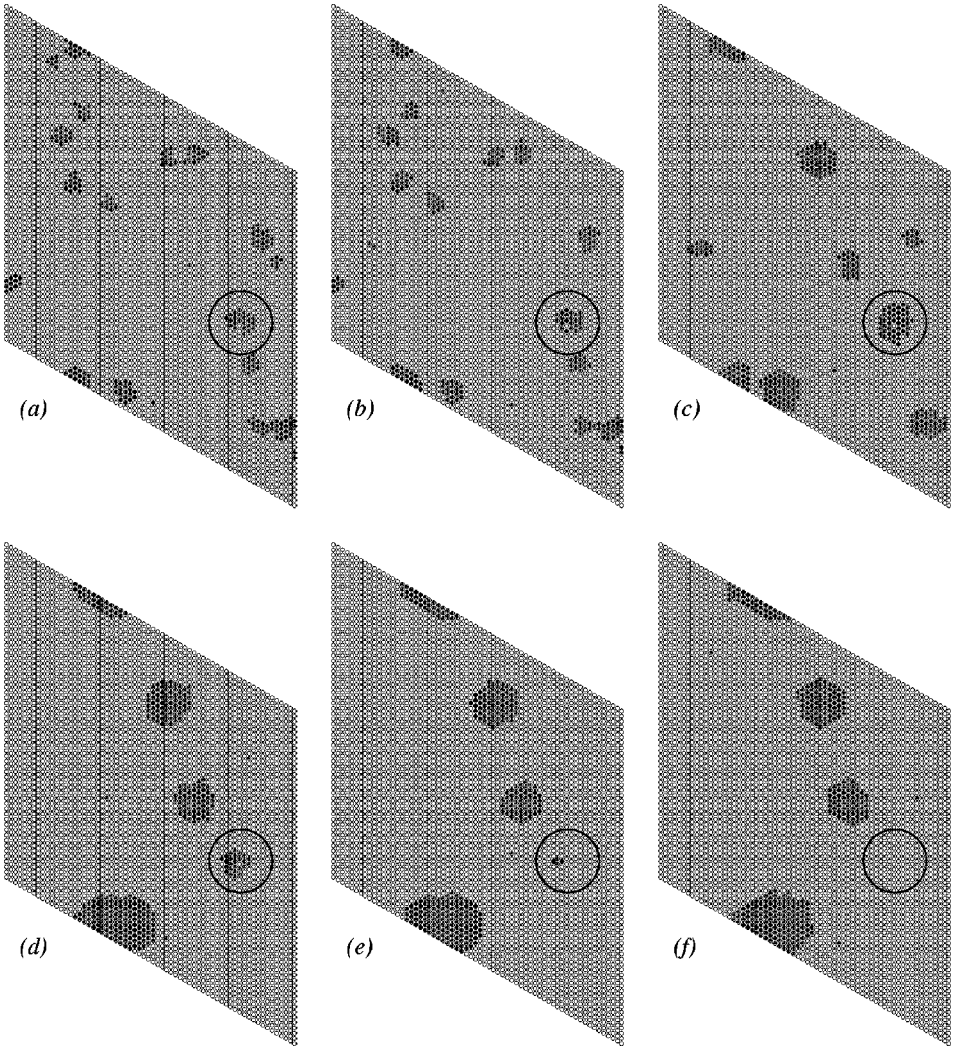

FIG. 8. Sequence of snapshots in a {111} plane (taken from a 3D 64^3 simulation box) showing a typical incorporation process of one A solvent atom (see text) at $T=0.258T_c$ for $a^*=-1$ and with $c=0.05$, during the kinetics at $L(t)=79$ (a), 81 (b), 214 (c), 688 (d), 726 (e), 817 (f) atoms. B atoms are represented as dark circles.

solute atoms. This suggests that for some kinetic reasons the vacancy, when $a^* \leqslant -1$, has a tendency to cover with B solute atoms the A atoms trapped at the interface (hereafter referred to as chemical interface defects), while when $a^* \geqslant -0.5$ the vacancy has a tendency to anneal these chemical interface defects. To test this assumption, we estimate the probabilities to observe these two events for two simple configurations.

Figure 9(a) shows schematically a typical interface chemical defect, which is susceptible to be transformed into an A atom trapped inside the precipitate. This chemical defect can be obtained by exchanging an AB pair from a perfect interface. Per interface site, its formation energy depends on the interface curvature and on ϵ. For a cubo-octahedron precipitate and according to the notation from Sec. III A, this energy is $-(Z-Z^+-Z^-+1)\epsilon$ and increases with the cluster size. When this defect is formed, it consists of an A defect atom (noted A_d) presenting a low number (Z^+-1) of first-neighbor A atoms and one B adatom (noted B_d).

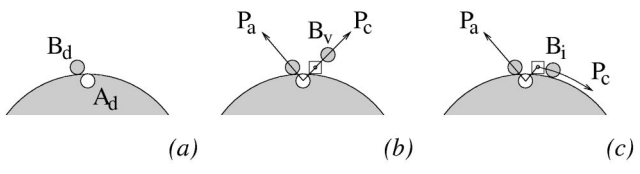

FIG. 9. Schematic B precipitate interface, where (a) a chemical defect A_dB_d is formed. The right sketches represent the two considered mechanisms by which a new solute atom, B_v (b) or B_i (c), covers partially the defect with a probability P_c. The vacancy involved (□) may also anneal the defect with a probability P_a.

In Figs. 9(b) and 9(c), we consider two possible mechanisms by which a new solute B atom covers partially the defect. This B atom may come either from the bulk [noted B_v in Fig. 9(b)] or from the cluster interface [noted B_i in Fig. 9(c)]. The coverage mechanism then requires a vacancy to be first neighbor of both A_d and B_v (or B_i). Among the various kinetic pathways of the vacancy, we consider two of them in Fig. 9 and calculate their probabilities: the vacancy exchanges first with B_v (or B_i) and then leaves the defect region with a probability P_c (mechanism to cover the defect), the vacancy exchanges first with A_d and then with B_d, with a probability P_a (mechanism to anneal the defect)

Calculations of probabilities P_a and P_c are detailed in Appendix B. To reduce the number of possible configurations we simplify the problem by taking a one-dimensional

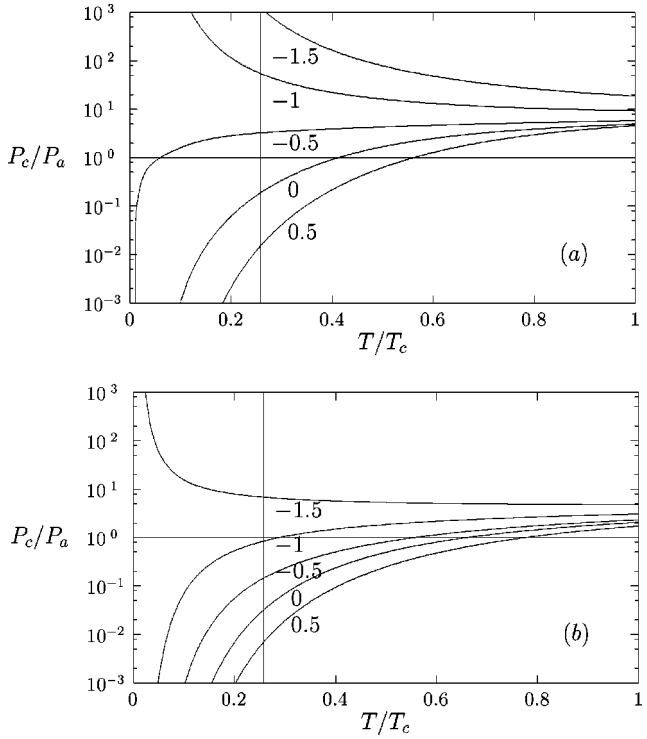

FIG. 10. P_c/P_a probability ratios as a function of the reduced temperature T/T_c, for various a^* values ($a^*=-1.5,-1,-0.5,0,0.5$) and for a cluster size $\langle l\rangle=100$ atoms. Calculations are obtained from Appendix B for the two cases involving: either (a) a B_v atom [Fig. 5(b)] or (b) a B_i atom [Fig. 5(c)].

model (i.e., with spherical symmetry) and by distinguishing only average residence time per concentric atomic shell. In this framework, the calculated probabilities however include reverse-jump probabilities in order to take into account the fact that some jumps are highly correlated.

The P_c/P_a calculation as a function of T/T_c and a^* is illustrated for $\langle l\rangle=100$ atoms in Figs. 10(a) and 10(b) for the cases involving a B_v and a B_i atom, respectively. At $T\approx 0.25T_c$ and for $a^*\leqslant -1$, both considered cases present very large P_c/P_a ratios, which, therefore, indicates a strong tendency to cover the chemical interface defect as observed in the KMC simulations. Conversely, for $a^*\geqslant 0$, the annealing of the interface defect is largely favored since P_c/P_a values are very small. Finally, the intermediate value $a^*=-0.5$ presents a competition between the two mechanisms depending on the type of B atom considered (B_v or B_i). Calculations reveal a small tendency to cover the chemical defect with a B_v atom and a small tendency to anneal it in presence of a B_i atom.

This simple calculation of P_c/P_a provides direct support for the qualitative explanation of the precipitate supersaturation origin. It confirms our conclusions made from the direct visualization of the configurations in Fig. 8 and it predicts the presence of supersaturated precipitates for $a^*<-0.5$ as observed in the Monte Carlo simulations in Fig. 6. Numerically, the drastic decrease of P_c/P_a when a^* increases comes from the fact that in the mechanism to cover the defect, the exchange of the vacancy with the B_v atom becomes highly correlated when a^* increases, i.e., the vacancy tends to jump straight back to its initial position when a^* increases.

This model also provides some insight into the buildup of interface roughness since the failure to anneal the above chemical defects correspond to a lack of interfacial diffusion that could smooth out interfacial roughness. This lack of interfacial diffusion can be seen as a generalization of the positive Ehrlich-Schwoebel barriers that are known to exist for the migration of B atoms across descending steps when $a^*\geqslant -1/3$.[33] The present situation is however more complex because of the curvature of the interface and because of the many successive configurations that are involved in the trapping of the A atoms. In qualitative agreement with the present calculations, it is observed in the KMC simulations (Fig. 7) that diffuse interfaces develop only for $a^*\leqslant -1$. A full treatment of the effect of a^* on the kinetic roughening of growing interfaces is however clearly beyond the reach of this simple model.

IV. DISCUSSION

In the past, most KMC studies of second-phase precipitation and coarsening have been performed with no interaction asymmetry ($a^*=0$). We show here that the kinetic path of precipitation is however strongly affected by moderate asymmetries, i.e., in the range of unity. For application to real alloy systems, one can choose to determine the asymmetry from the difference of the pure metal-cohesive energies, or the vacancy formation energies, or the vacancy migration energies. For metallic alloys different asymmetry parameters will be obtained depending upon the method used, because of the well-known failure of pair potentials to reproduce properly the energetics of these alloys. The main point is, however, that quite large values are often obtained,[10] for instance, ranging from $a^*=-1.8$ to -3 for Cu-Co. We therefore conclude that for many experimental situations the evolution of the system cannot be properly reproduced without taking into account asymmetry effects.

As a direct illustration of the above point, new three-dimensional atom probe measurements of the composition and interface properties of Co-rich precipitates growing at 723 K in a Cu-rich matrix have revealed unexpected features, such as the formation of supersaturated precipitates containing up to 20% Cu and the formation of disordered, diffuse interfaces extending over 1 nm.[18] These unexpected and so far unexplained features are directly reminiscent of our findings for moderate or large negative asymmetry parameters. The reduced experimental temperature is larger than that used in the present simulations: by fitting the solubilities with a subregular solution model this reduced temperature is estimated to be $\approx 0.45T_c$.[34] The asymmetry parameter for the Cu-Co system is however more negative than the values we used in our simulations. Our mean-field model indicates that both variations (T and a^*) in fact compensate each other, and that asymmetry effects for Cu-Co at 723 K are expected to be similar to that observed in our simulations for

$-1.5 \leqslant a^* \leqslant -1$. Simulations with an improved kinetic model (see Sec. II) and parameters close to the experimental conditions are in progress to allow for a quantitative comparison.

V. CONCLUSION

In this paper we investigate the effect of asymmetric atomic mobilities on the precipitation path in a model binary alloy. We use an atomistic model where energetics is simply modeled by first nearest-neighbor pair interactions, and where diffusion proceeds by atom-vacancy exchanges. Results obtained using kinetic Monte Carlo simulations show that the interaction asymmetry parameter, $a^* = (\epsilon_{AA} - \epsilon_{BB})/(\epsilon_{AA} + \epsilon_{BB} - 2\epsilon_{AB})$, has a determinant impact on the precipitation kinetics and on the characteristics of the precipitates that are formed during isothermal annealing. For a $A_{95}B_5$ alloy quenched from infinite temperature and annealed at $T = 0.258 T_c$ we found the following.

(1) The coarsening of the precipitate is quickly dominated by the evaporation-condensation mechanism for $a^* \leqslant -0.5$, while for $a^* \geqslant 0$ the coagulation mechanism remains the dominant coarsening mechanism for precipitate sizes at least up to 1000 atoms. Furthermore, in the coagulation regime, the volume-coarsening exponent increases from about 0.33 for $a^* = -0.5$ to 0.62 for $a^* = 0.5$.

(2) For $a^* = 0, -0.5$ the compositions of the precipitates and of the matrix are in good agreement with the (local) equilibrium compositions predicted by the Gibbs-Thomson formula. In the case $a^* \leqslant -1$, however, a large supersaturation of the precipitates is measured (more than two orders of magnitude), while in the case $a^* = 0.5$ a significant supersaturation of the matrix persists for long times.

(3) In the case where supersaturated precipitates are observed, precipitate/matrix interfaces are shown to carry a large energy excess, which originates from disordered, rough interfaces.

We have shown that these results can be rationalized when one takes into account the effect of the asymmetry parameter on the vacancy distribution and migration in an alloy that contains precipitates. Using a simple mean-field model we show in particular that by varying a^* one can force the vacancy to reside mostly in the matrix (for large negative a^* values) or to be trapped in the precipitates (for large positive a^* values). Furthermore, the vacancy probability distributions display different evolutions with the precipitate size. These combined effects provide a simple qualitative explanation for the effect of a^* on coarsening mechanisms and even a quantitative modeling for the coagulation exponents. We then propose a simple mean-field kinetic model to study the effect of a^* on the trapping of A atoms at growing precipitate interfaces. The model, in agreement with the KMC simulations, indicates that when $a^* \leqslant -1$, A atoms are kinetically trapped at growing interfaces. This provides a simple explanation for the buildup of interface roughness and the precipitate supersaturations measured in the simulations.

ACKNOWLEDGMENTS

It is a pleasure to thank A. Saúl and G. Tréglia for their stimulating discussions. This work was supported by the U.S. Department of Energy Grant No. DEFG02-96ER45439 through the University of Illinois Materials Research Laboratory. The present simulation work has greatly benefited from the MRL Center for Computation.

APPENDIX A: CUBO-OCTAHEDRON CLUSTER

To quantify the various geometric parameters describing a typical cluster considered in Sec. III A, we have used a simple cubo-octahedral polyhedron in the fcc structure. In this appendix we detail this numerical aspect.

Cluster surface and volume. Consider n, the number of successive atomic shells forming a cubo-octahedron of B atoms embedded in a matrix of A atoms. The cluster surface then contains $N_s(n) = 2(5n^2 + 1)$ atoms which, by summing each shell gives a cluster volume $N_{tot}(n) = 1 + (n/3)(10n^2 + 15n + 11)$ atoms. For numerical application in Eq. (5) we take $\langle l \rangle = N_{tot}(n)$, $\langle l \rangle - \langle l^- \rangle = N_s(n)$, and $\langle l^+ \rangle - \langle l \rangle = N_s(n+1)$.

Coordination number. Each shell presents four inequivalent types of sites [on vertex, edges, (100) and (111) faces]. Taking into account these different sites, the nth shell shares with the $(n+1)$th one, a number of bonds $N_{n|n+1} = 12(3n^2 + 3n + 1)$. To estimate Z^- and Z^+ in Eqs. (6) and (7), we distinguish for a site in a given shell the number of its first neighbors in adjacent and same shells. Thus, a site in the surface shell (i.e., the nth shell) has an average number of first neighbors in the adjacent $(n+1)$th shell $Z_n^+ = N_{n|n+1}/N_s(n)$, in the adjacent $(n-1)$th shell $Z_n^- = N_{n-1|n}/N_s(n)$, and in the same nth shell $Z_n^0 = Z - Z_n^+ - Z_n^-$, where $Z = 12$ is the total fcc coordination number. In Eqs. (6) and (7) $Z^- = Z_{n+1}^-$ and $Z^+ = Z_n^+$.

APPENDIX B: P_c/P_a CALCULATION

We detail in this appendix the calculation of P_c/P_a probability ratio discussed in Sec. III C 2. It requires us to define average atom-vacancy exchange frequencies at the vicinity of the cluster interface and for the specific configurations considered in Figs. 9.

Average frequencies and residence times. Using average coordination number from the above described cubo-octahedron geometry, we report for various atom-vacancy exchanges in Table III the configuration dependent part of the activation energies defined in Eq. (1). In Table III, indices p denote the shell where the element A_p, B_p, or V_p is located. Considering, for example, the exchange between a vacancy in the nth shell (V_n) and an A atom in $(n+1)$th shell (A_{n+1}), this A atom is surrounded by $(Z - Z_{n+1}^-)$ A first-neighbor atoms, and according to Eq. (1), the frequency for this exchange is

$$\Gamma\{V_n A_{n+1}\} = \nu \exp\left\{ - \frac{E^0 - \frac{1}{2}(Z - Z_{n+1}^-)(1 + a^*)\epsilon}{kT} \right\}. \tag{B1}$$

TABLE III. Configuration-dependent part of the activation energies [Eq. (1)] for vacancy-atom exchanges in the vicinity of a cubo-octahedron cluster interface, where $E_{VB}=(\epsilon/2)(1+a^*)$ and $E_{VA}=(\epsilon/2)(1-a^*)$. Coordination numbers $(Z_n^-, Z_n^+, \ldots)$ are defined in Appendix A. Indices p denote the shell where the element A_p, B_p, or V_p is located (see Appendix B). In the lower part of the table, the specific exchanges in the configurations illustrated in Fig. 9 are considered.

	V_{n-1}	V_n	V_{n+1}	V_{n+2}
A_{n+2}			$[Z-1]E_{VB}$	$-[Z-1]E_{VB}$
A_{n+1}		$-[Z-Z_{n+1}^-]E_{VB}$	$-[Z-Z_{n+1}^--1]E_{VB}$	$-[Z-Z_{n+1}^--1]E_{VB}$
B_n	$-[Z-Z_n^+-1]E_{VA}$	$-[Z-Z_n^+-1]E_{VA}$	$-[Z-Z_n^+]E_{VA}$	
B_{n-1}	$-[Z-1]E_{VA}$	$-[Z-1]E_{VA}$		
A_d		$-[Z-Z_{n+1}^--1]E_{VB}$	$-[Z_n^+-2]E_{VB}$	
B_d		$-[Z_{n+1}^--1]E_{VA}$		
B_v			0	$-[Z_{n+1}^--1]E_{VA}$
B_i		$-[Z_{n+1}^--1]E_{VA}$	$-[Z_{n+1}^-]E_{VA}$	$-[Z_{n+1}^-]E_{VA}$

From Table III, the mean residence time τ of the vacancy in this configuration can be written as

$$\tau=[Z_n^-\Gamma\{V_nB_{n-1}\}+Z_n^0\Gamma\{V_nB_n\}+Z_n^+\Gamma\{V_nA_{n+1}\}]^{-1}. \tag{B2}$$

Let us now consider the specific configurations illustrated in Fig. 9, i.e., a vacancy V_{n+1} that is first neighbor of both A_d and B_v (or B_i) atoms. We note τ_0^v and τ_0^i, the mean residence times of the vacancy [respectively, in Figs. 9(b) and 9(c)] before making any first jump. V_{n+1} is assumed not to be first neighbor of B_d and therefore has Z_{n+1}^-B first neighbors. To simplify the calculation, only the local environments of this initial vacancy site and of the A_d, B_v (or B_i) ones are considered. Average coordinations of the other neighbor atoms are given by the cubo-octahedron geometry.

Probability P_a to anneal the defect. As defined in Sec. III C 2 and illustrated in Fig. 9, P_a is the probability for a vacancy V_{n+1} to exchange first with A_d and then with B_d. P_a may be written as the product of two relative probabilities

$$P_a=\Gamma\{V_{n+1}A_d\}\tau_0\times\Gamma\{V_nB_d\}\tau_a, \tag{B3}$$

where $\tau_0=\tau_0^v$ (or τ_0^i) and τ_a is the mean residence time after the first vacancy jump. Using the above mentioned approximation to calculate average frequencies, the activation energies for $\Gamma\{V_{n+1}A_d\}$ and $\Gamma\{V_nB_d\}$ are reported in Table III and τ_a is given by

$$\tau_a=[Z_n^-\Gamma\{V_nB_{n-1}\}+Z_n^0\Gamma\{V_nB_n\}+(Z_n^+-2)\Gamma\{V_nA_{n+1}\}+\Gamma\{V_nA_d\}+\Gamma\{V_nB_d\}]^{-1}, \tag{B4}$$

where $\Gamma\{V_nA_d\}$ is the frequency of the reverse $V_{n+1}A_d$ exchange.

Probability P_c to cover the defect. P_c^v (P_c^i) is the probability for the vacancy V_{n+1} to exchange first with B_v (B_i) and then with any A atoms (see Sec. III C 2 and Fig. 9). Considering the mechanism involving B_v, we have

$$P_c^v=\Gamma\{V_{n+1}B_v\}\tau_0^v\times[1-\Gamma\{V_{n+2}B_v\}\tau_c^v], \tag{B5}$$

where $\Gamma\{V_{n+2}B_v\}$ is the frequency of the reverse $V_{n+1}B_v$ exchange and τ_c^v is the mean residence time after the first jump,

$$\tau_c^v=[(Z_{n+2}^--1)\Gamma\{V_{n+2}A_{n+1}\}+\Gamma\{V_{n+2}B_v\}+(Z-Z_{n+2}^-)\Gamma\{V_{n+2}A_{n+2}\}]^{-1}. \tag{B6}$$

Similarly, for the mechanism with B_i,

$$P_c^i=\Gamma\{V_{n+1}B_i\}\tau_0^i\times[(Z_{n+1}^0-1)\Gamma\{V_{n+1}A_{n+1}\}+Z_{n+1}^+\Gamma\{V_{n+1}A_{n+2}\}]\tau_c^i, \tag{B7}$$

where τ_c^i is the mean residence time after the first jump

$$\tau_c^i=[Z_{n+1}^-\Gamma\{V_{n+1}B_n\}+(Z_{n+1}^0-1)\Gamma\{V_{n+1}A_{n+1}\}+\hat{\Gamma}\{V_{n+1}B_i\}+Z_{n+1}^+\Gamma\{V_{n+1}A_{n+2}\}]^{-1}, \tag{B8}$$

where $\hat{\Gamma}\{V_{n+1}B_i\}$ is the frequency of the reverse $V_{n+1}B_i$ exchange, which differs from $\Gamma\{V_{n+1}B_i\}$ only by the fact that B_i has now (Z_{n+1}^--1) B neighbors (due to the presence of A_d) instead of Z_{n+1}^-.

In Figs. 10(a) and 10(b), respectively, ratios P_a/P_c^v and P_a/P_c^i are plotted as functions of the temperature and for a cluster size $\langle l\rangle=100$ atoms. Notice that in Eqs. (B3)–(B7) probabilities can be modified by the fact that the vacancy may also perform other correlated (and more complicated) jump sequences driven by the a^* asymmetry term. In particular, before doing its first jump, the vacancy may return to its initial site after any two reverse jumps and without changing the atomic configuration. It is however interesting to note that this contribution enhances by the same factor the probabilities P_a, P_c^i, and P_c^i,[12] and therefore, does not affect their ratios reported in Fig. 10.

[1] J. D. Gunton, M. San Miguel, and P. S. Sahni, in *Phase Transitions and Critical Phenomena*, edited by C. Domb and J. L. Lebowitz (Academic, New York, 1983), Vol. 8.
[2] R. Wagner and R. Kampmann, in *Phase Transformations in Materials*, edited by P. Haasen (VCH, Weinheim, 1991).
[3] I. M. Lifshitz and V. V. Slyozov, J. Phys. Chem. Solids **19**, 35 (1961).
[4] C. Wagner, Z. Elektrochem. **65**, 581 (1961).
[5] K. Binder and D. Stauffer, Phys. Rev. Lett. **33**, 1006 (1974).
[6] K. Binder, Phys. Rev. B **15**, 4425 (1977).
[7] J. Philibert, *Atom Movements: Diffusion and Mass Transport in Solids* (Editions de Physique, Les Ulis, France, 1991).
[8] P. Fratzl and O. Penrose, Phys. Rev. B **55**, R6101 (1997).
[9] T. T. Rautiainen and A. P. Sutton, Phys. Rev. B **59**, 13 681 (1999).
[10] B. Legrand (private communication).
[11] M. Athènes, P. Bellon, G. Martin, and F. Haider, Acta Mater. **44**, 4739 (1996).
[12] M. Athènes, P. Bellon, and G. Martin, Philos. Mag. A **76**, 565 (1997).
[13] M. Athènes and P. Bellon, Philos. Mag. A **79**, 2243 (1999).
[14] M. Porta, C. Frontera, E. Vives, and T. Castan, Phys. Rev. B **56**, 5261 (1997).
[15] M. Porta, E. Vives, and T. Castan, Phys. Rev. B **60**, 3920 (1999).
[16] M. Athénes, P. Bellon, and G. Martin, Acta Mater. **48**, 2675 (2000).
[17] F. Soisson and G. Martin, Phys. Rev. B **62**, 203 (2000).
[18] I. Rozdilsky, Ph.D. thesis, Oxford University, 1998; I. Rozdilsky, A. Cerezo, G. D. W. Smith, and A. Watson, in *Phase Transformations and Systems Driven Far from Equilibrium*, edited by E. Ma, P. Bellon, M. Atzmon, and R. Trivedi, MRS Symposia Proceedings No. 481 (Materials Research Society, Pittsburgh, 1998), p. 521.
[19] F. Soisson, A. Barbu, and G. Martin, Acta Mater. **44**, 3789 (1996).
[20] A. Bieber, F. Gautier, G. Tréglia, and F. Ducastelle, Solid State Commun. **39**, 149 (1981).
[21] G. Martin, Phys. Rev. B **41**, 2279 (1990).
[22] See, for example, M. E. Fisher, Rep Prog. Phys. **30**, 615 (1967).
[23] P. Ehrhart, P. Jung, H. Schultz, and H. Ullmaier, in *Atomic Defects in Metals*, edited by H. Ullmaier, Landolt-Börnstein, New Series, Group III, Vol. 25 (Springer-Verlag, Berlin, 1991).
[24] A. B. Börtz, M. H. Kalos, and J. L. Lebowitz, J. Comput. Phys. **17**, 10 (1975).
[25] M. A. Novotny, Comput. Phys. **9**, 46 (1995).
[26] P. Mirold and K. Binder, Acta Metall. **25**, 1435 (1977).
[27] See, for example, P. Wynblatt and R. C. Ku, *Interfacial Segregation* (American Society for Metals, Metals Park, OH, 1977), p. 115.
[28] See, for example, W. Romanowski, Surf. Sci. **18**, 373 (1969); C. Mottet, Ph.D. thesis, University of Aix-Marseille II, 1997.
[29] D. Le Floc'h, P. Bellon, and M. Athènes, Phys. Rev. B **62**, 3142 (2000).
[30] P. Fratzl, O. Penrose, R. Weinkamer, and I. Žižak, Physica A **279**, 100 (2000).
[31] J. S. Langer, M. Bar-On, and H. D. Miller, Phys. Rev. A **11**, 1417 (1975).
[32] J. M. Roussel and P. Bellon (unpublished).
[33] P. Bellon, Phys. Rev. Lett. **81**, 4176 (1998).
[34] R. P. Setna, Ph.D. thesis, Oxford University 1994.